ORIGINAL PAPER

Co-electrodeposition of MnO$_2$/graphene oxide coating on carbon paper from phosphate buffer and the capacitive properties

Hua Zhao · Feifei Liu · Gaoyi Han · Zhaoyang Liu ·
Bin Liu · Dongying Fu · Yanping Li · Miaoyu Li

Abstract MnO$_2$/graphene oxide sheet composite (MnO$_2$/GOS) has been co-electrodeposited on the thermally treated carbon paper (TTCP) in phosphate buffer solution containing GOS and KMnO$_4$. The resulted samples have been characterized by scanning and transmission electron microscopy, Raman, X-ray diffraction, and X-ray photoelectron energy spectroscopy. The results show that the synthesized MnO$_2$ may be δ-MnO$_2$ and the morphology of MnO$_2$/GOS is very different from that of MnO$_2$, indicating that the introduction of GOS in electrolyte can influence the morphology during the deposition. The capacitive properties of the samples are investigated by using cyclic voltammetry, galvanostatic charge/discharge, and electrochemical impedance spectroscopy. The specific capacitance of MnO$_2$ for MnO$_2$/GOS can reach about 829 F g^{-1} at discharged current density of 1.0 A g^{-1} in 1 M Na$_2$SO$_4$ aqueous solution, which is larger than that of MnO$_2$ deposited on TTCP. The composite of MnO$_2$/GOS also exhibits excellent cyclic stability with a decrease of 18.5 % specific capacitance after 1,500 cycles.

H. Zhao · F. Liu · G. Han (✉) · Z. Liu · B. Liu · D. Fu · Y. Li · M. Li
Institute of Molecular Science, Key Laboratory of Chemical Biology and Molecular Engineering of Education Ministry, Shanxi University, Taiyuan 030006, China
e-mail: han_gaoyis@sxu.edu.cn

Introduction

Electrochemical capacitors, known as a kind of electrical charge-storage devices, have attracted tremendous attention because of their high power density, excellent reversibility, and cycle life [1, 2]. Based on the operating mechanisms, electrochemical capacitors can be generally classified into two kinds: one is the double-layer capacitors which depend on the charge-separation at the interface of the electrode's materials and electrolyte; the other is pseudocapacitors which depend on the Faradic redox reaction of the electrochemically active materials. Recently most research about the materials of electrode has focused on the development of electrochemically active materials including various carbon materials, conducting polymers, and transition metal oxides [3–6].

Among the electrochemically active materials, manganese oxide is considered as a promising material due to its low cost, high electrochemical activity and environment-friendly nature [5, 6]. Although MnO$_2$ possesses high specific capacitance (C_{cs}) in theory (1,370 F g^{-1}) [7, 8], the values of C_{cs} for the synthesized MnO$_2$ usually range from 100 to 400 F g^{-1} [9, 10] because the capacitive reaction of MnO$_2$ can only occur on the surface due to its poor conductivity. Therefore, the architecture for hybrid electrode has been developed to improve the performance of electrodes. Thin MnO$_2$ film is usually deposited on high-surface-area conductive supports to increase its surface area and mass loading, and to improve the conductivity of the material [11, 12].

Up to date, the composites of MnO$_2$ and carbon materials such as carbon nanotubes and carbon paper have been synthesized and measured for their capacitive properties [13–17]. Graphene is regarded as promising material in

consideration of its excellent conductivity, large specific surface area and good mechanical property [18, 19], so some composites of MnO_2 and graphene have also been fabricated [20–23], and the results demonstrate that the addition of graphene can improve the capacitive performance. Besides the precipitation, hydrothermal and sol–gel processes, electrochemical deposition is a convenient method to deposit MnO_2 on conductive substrates by anodic or cathode process when Mn^{2+} or MnO_4^- are used as precursors [6, 24–27].

Recently, the composite of MnO_2 and graphene has also been fabricated by electro-depositing MnO_2 on the layer of electrochemically reduced graphene through anodic process, and the C_{sc} of the composite was reported to be about 122 F g^{-1} [28]. The co-deposition of MnO_2 and graphene or GOS through anodic process is difficult because Mn^{2+} or high concentration of Na_2SO_4 will agglomerate the GOS in the aqueous solution. However, in the phosphate buffer solution (PBS), the dispersion of GOS is stable although the concentration of $KMnO_4$ is relatively high. On the other hand, GOS can be electrochemically reduced to graphene in phosphate buffer solution (PBS) at negative potential [29, 30]. Considering the above-mentioned factors, the hybrid of MnO_2/GOS will be co-deposited on thermally treated carbon papers (TTCP) by using cyclic voltammetry (CV) in PBS containing $KMnO_4$ and GOS. It is expected that the obtained product exhibits high capacitive performance.

Experiment

The deposition of MnO_2/GOS composite on carbon paper

According to literatures [31, 32], GOS was synthesized from the powdered flake graphite (325 mesh). The commercial carbon papers (CP, Toray Composites Inc, Japan) were thermally treated in a muffle furnace at 550 °C under the atmospheric atmosphere for 1 h firstly, and then in a muffle furnace at 550 °C in air for 3 h again after being heated at 1,200 °C for 2 h in a tube furnace under Ar atmosphere (TTCP). During the process of treatment, the surface of carbon fibers was activated by oxygen in air at 550 °C firstly, and the formed activated groups were removed at 1,200 °C under Ar atmosphere and then more sites were left on the surface after the activation again in air at 550 °C [33, 34]. It was expected that the carbon fibers exhibit larger surface area and more hydrophilic by this treatment. The reagent of $KMnO_4$ and others were analytical grade without further purification.

The GOS powder was exfoliated in 0.067 mol L^{-1} PBS (pH=9.18) under ultrasonic condition to form colloidal dispersion of GOS (1.0 mg mL^{-1}) firstly, then $KMnO_4$ was dissolved into the dispersion of GOS to form the electrolyte (C_{KMnO4}=3.0 mg mL^{-1}). The strips of TTCP (20 mm×3 mm) fixed on the copper bar, Pt plate, and saturated calomel

electrode (SCE) were used as the working, counter, and reference electrodes, respectively. The electro-deposition was carried out on CHI 660C electrochemical station (Chenhua, Shanghai) by CV method, the potential window ranged from 0.8 to −0.15 V and the scan rate was 100 mV s^{-1}. The obtained sample was named as TTCP-MnO_2/GOS and the mass loading of MnO_2 was about 0.43 mg cm^{-2} based on the geometric surface area of the electrode. In order to make a comparison, the sample defined as TTCP-MnO_2 was also prepared under the same condition but without GOS in the electrolyte.

Characterization and electrochemical measurements

The morphologies of the samples were observed on a JSM-6701F scanning electron microscope (SEM) operating at 10 kV and transmission electron microscopy (TEM, JEOL 2010) operating at 200 kV. For measurements of TEM, the samples deposited on TCCP were peeled in water by ultrasonic. The X-ray diffraction (XRD) patterns were recorded on a Bruker D8 Advance X-ray diffractometer (CuKα) in the 2 theta range of 5°–80° by using grazing incidence accessories. The X-ray photoelectron spectroscopy (XPS) was performed on an American Thermo-VG Scientific ESCALAB 250XPS system with Al Kα radiation as the exciting source. Raman spectra were recorded on a JobinYvon Lab RAMHR800 microscopic confocal Raman spectrometer by using laser of 514.5 nm as incident light. To have a high signal-to-noise ratio, each spectrum was the average of 8 successive scans, and to avoid sample photodecomposition or denaturation, the spectra were recorded using a low excitation power of 10 mW.

The capacitive properties of the electrodes were evaluated on CHI 660C electrochemical station by using TTCP-MnO_2/GOS and TTCP-MnO_2 fixed on copper rods, Pt plate, and SCE electrodes as working, counter and reference electrode in 1.0 mol L^{-1} Na_2SO_4 aqueous solution. The CV curves were recorded in a potential range of −0.1 to 0.8 V at various scan rates. Charge/discharge curves were recorded at different current densities with the cutoff voltage between −0.1 and 0.8 V. The electrochemical impedance spectra (EIS) were measured in the range of 10^5–10^{-2} Hz at open-circuit with ac-voltage amplitude of 5 mV.

Results and discussion

The characterization of the materials

The CV curves during the process of electro-deposition for MnO_2/GOS are shown in Fig. 1a, from the curve of first cycle, it is clear to find that MnO_4^- can be reduced at about 0.51 V and that the reduction current increases with the decrease of

Fig. 1 (**A**) CV deposition process of the MnO$_2$/GOS on the TTCP in PBS containing 0.5 mg mL^{-1} GOS. (**B**) XRD patterns of MnO$_2$ (**a**), MnO$_2$/GOS hybrid (**b**), TTCP-MnO$_2$/GOS (**c**), and TTCP (**d**). (**C**) Mn2p XPS peaks of MnO$_2$/GOS hybrid. (**D**) The C1s XPS peaks of GOS (**a**) and MnO$_2$/GOS hybrid (**b**). (**E**) The Raman spectra of GOS (**a**), MnO$_2$ (**b**), and MnO$_2$/GOS (**c**)
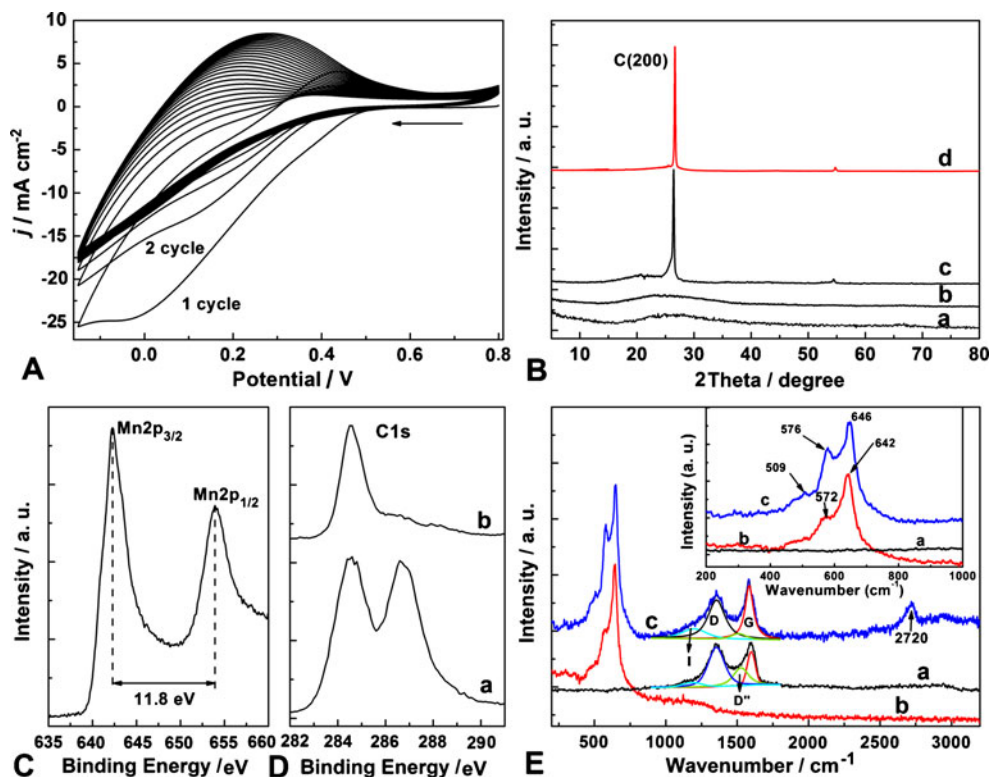
potential during the negative scan, while an oxidative wave appears at about 0.40 V during the positive scan, which indicates that MnO$_2$ has deposited on the surface of TTCP. With the process proceeding, the oxidative waves shift to about 0.25 V and the peak current densities increase, revealing that more amounts of MnO$_2$/GOS has been deposited on the surface of TTCP. It is surprising to find that the strong diffraction peak of C (002) appears in the XRD pattern of TTCP-MnO$_2$/GOS (Fig. 1B—c) but no obvious diffraction

peaks are related to MnO$_2$. However, it can be found carefully that the TTCP-MnO$_2$/GOS shows a weak broad peak near the C(200) diffraction peak compared with the XRD pattern of TTCP (Fig. 1B—d). In order to clarify the products, the synthesized MnO$_2$ and MnO$_2$/GOS hybrid are scraped from the electrode and measured. Both the XRD patterns show weak and broad peaks at about 18°–36° (Fig. 1B—a, b), indicating that the synthesized MnO$_2$ exhibits very small particles or is amorphous.

Fig. 2 The micrographs of the samples, SEM images of TTCP (**A**), TTCP-MnO$_2$ (**B**), and TTCP-MnO$_2$/GOS (**C**). The TEM images of MnO$_2$ (**D**) and MnO$_2$/GOS (**E**). The *inserted figures* in SEM images are the low magnified images, and the *inserted figures* in TEM images are the low magnified images and the patterns of selected area electron diffraction
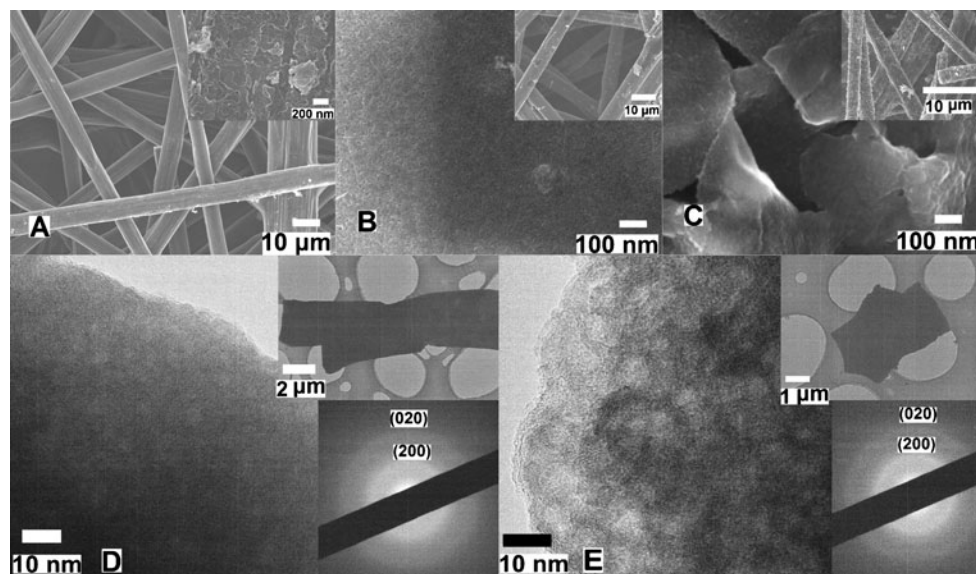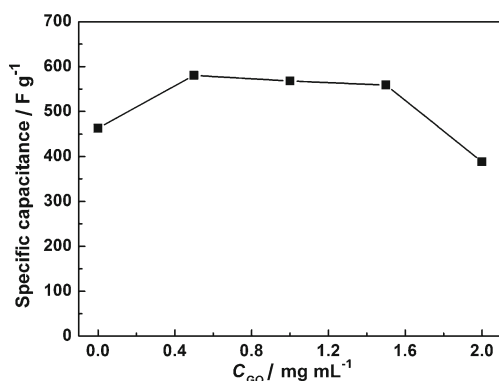
Fig. 3 The plot of specific capacitance of MnO_2 versus the concentration of GO in the electrolyte

In order to clarify the valence state of Mn, the XPS spectra are recorded and shown in Fig. 1C. From the XPS peaks of Mn2p, it is found that the peaks of $Mn2p_{3/2}$ and $Mn2p_{1/2}$ are located at about 642.9 and 654.7 eV, the difference between them is about 11.8 eV, indicating that the main product deposited on the carbon substrates is MnO_2 [11]. The C1s XPS spectrum of GOS shows two peaks at 284.5 and 287.0 eV which can be assigned to the C–C bond and the oxygen-containing groups such as C–O, COOR, and C=O (Fig. 1D—a), respectively. However, the sample of $MnO_2/$GOS shows weak peaks related to C–C bond and oxygen-containing groups in contrast with GOS [35]. The Raman spectra of the GOS, MnO_2 and $MnO_2/$GOS are shown in Fig. 1E. It is found that the GO shows two broad bands (Fig. 1E—a). According to the literature [36], the two bands can be fitted by four components, the G band (1,598 cm^{-1}) is attributed to all sp^2 carbon forms and provides information on the in-plane vibration of sp^2 bonded carbon atoms while the D band (1,354 cm^{-1}) suggests the presence of sp^3 defects [31]. The components centered near 1,522 and 1,190 cm^{-1} are called D″ and I bands, respectively, but they have uncertain origins [36]. The spectrum of the electro-synthesized MnO_2 exhibits the peaks at the region of 400–800 cm^{-1} (Fig. 1E—b), which are attributed to the stretching mode of the MnO_6

octahedra [37].The band around 642 cm^{-1} could be attributed to the symmetric stretching vibration (Mn–O) of the MnO_6 groups, while the peak at 572 cm^{-1} could be due to the Mn–O stretching in the basal plane of the MnO_6 sheet [37]. According to the literatures [37, 38], it can be deduced that the synthesized MnO_2 may be birnessite. However, the sample of $MnO_2/$GOS exhibits the peaks of MnO_2 and GOS (Fig. 1E—c), the peaks corresponding to the MnO_2 shift to high wavenumber slightly, which may be attributed to the presence of GOS. It is found that the intensity of G band in sample of $MnO_2/$GOS become stronger compared with that in GOS, and that the D/G value (the area ratio of D to G band) for $MnO_2/$GOS (1.36) is smaller than that for GOS (2.28), indicating that the defects have become less and the GOS may be partially reduced during the process of electrodeposition. Furthermore, the obvious 2D peak suggests that the GOS are separated well by the formed MnO_2. Considering that the GO is electrochemically reduced at potential of −1.0 to 1.5 V and the potential in our experiment is arranged at −0.15 to 0.8 V, so we can deduce that GOS may be partially reduced during the deposition process according to the fact that C1s XPS peak related to the oxygen-containing groups has become weak and that the value of D/G has become small according to the Raman spectra.

From the images of the micro-morphologies shown in Fig. 2, it is found that the surface of the fibers in TTCP is rough and the diameter of the fibers ranges from several to more than 10 microns (Fig. 2A), and many small holes are observed on the surface of the fibers. The surface of the fibers in TTCP-MnO_2 becomes smooth and the fibers are coated by porous layer of MnO_2 formed by small MnO_2 particles (Fig. 2B), and the outer and inner fibers are coated with the MnO_2 layer (inserted figure). However, the morphology of TTCP-$MnO_2/$GOS is very different from TTCP-MnO_2, the GOS coated with MnO_2 agglomerates together to form a fluffy layer on the surface of fibers, many gaps or pores are dispersed on the layer of $MnO_2/$GOS (Fig. 2C). The TEM images show that the MnO_2 and $MnO_2/$GOS deposited on TTCP are flakes, and that the MnO_2 (Fig. 2D) deposited on

Fig. 4 CV curves of TTCP-$MnO_2/$GOS at different scan rates (**A**), the plots of the specific capacitance of MnO_2 for TTCP-MnO_2 (**a**) and TTCP-$MnO_2/$GOS (**b**) versus the scan rates (**B**)
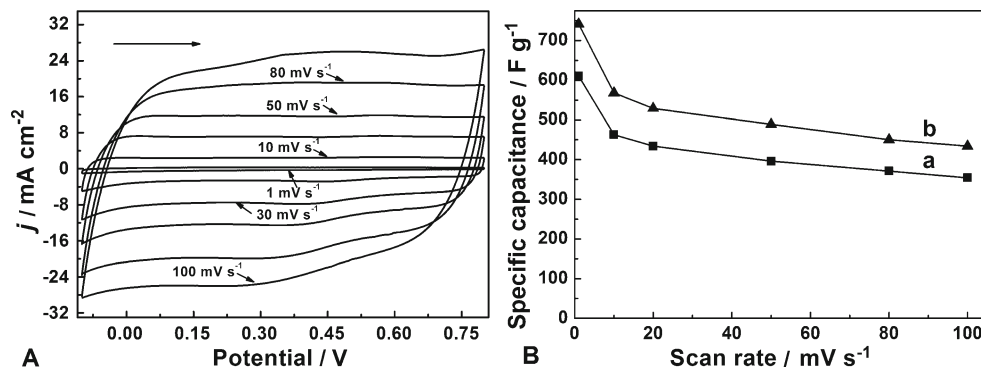
Fig. 5 The discharged curves of TTCP-MnO$_2$/GOS at various current densities (A) and the cycling charge/discharge curves (B) for TTCP-MnO$_2$/GOS (a) and TTCP-MnO$_2$ (b) at the current density of 5 A g^{-1}
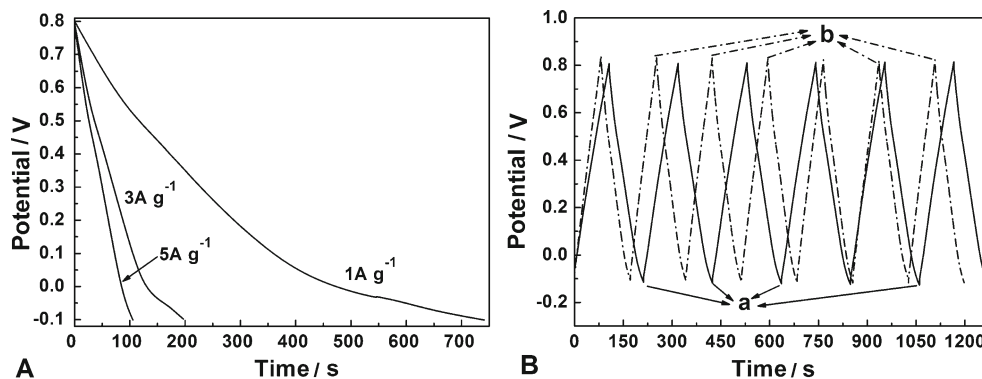
TTCP exhibits denser structure than MnO$_2$/GOS (Fig. 2E). The magnified image of MnO$_2$/GOS shows that distance between the GOS layers is about 0.35 nm (SFig. 1). It is found that two diffraction rings are appeared in the patterns of selected area electron diffraction for MnO$_2$ and MnO$_2$/GOS. It can be calculated that the distances between the planes are about 0.143 and 0.252 nm, which can be corresponded to the (020) and (200) planes in δ-MnO$_2$.

Figure 3 shows the relationship between the values of C_{cs} of MnO$_2$ and concentrations of GOS in the electrolyte. It is found that the value of C_{cs} for MnO$_2$ increases with the increase of GOS concentration and reaches the maximum and keeps a plateau when the concentration of GOS ranges from 0.5 to 1.5 mg mL^{-1}. The MnO$_2$/GOS obtained by this method possesses relatively higher values of C_{cs} than that of MnO$_2$ at the optimum conditions, which may be attributed to the high dispersion of MnO$_2$ on GOS and the porous structure formed on the TTCP. On the other hand, it is well known that GOS will agglomerate in the presence other reagents such as salts or when its concentration is high. The high content of GOS will aggregate and make the surface area decreased and cause the size of MnO$_2$ particles large [39]. Therefore, the GOS will facilitate the dispersion of in the optimum concentrations, and the PBS containing 1.0 mg mL^{-1} GOS
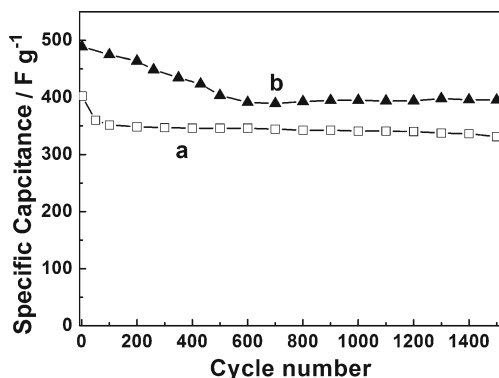
and 3.0 mg mL^{-1} KMnO$_4$ is chosen as electrolyte in the following experiments.

The electrochemical properties

The CV curves of TTCP-MnO$_2$/GOS at various scan rates are shown in Fig. 4A, it is found that the CV curves do not show obvious redox peaks corresponding to MnO$_2$ in the whole voltage range, indicating that the electrode is charged or discharged at a pseudo-constant rate during the whole CV process. The shapes of the curves are rectangular-like with the almost symmetric I–E responses when the scan rates are lower than 100 mV s^{-1}, indicating that there is the rapid current response on voltage reversal at each end potential, which accords with the ideal capacitive behavior. The shapes of CV curves for TTCP-MnO$_2$ are similar to that for TTCP-Mn/GOS, but exhibit small current density at the same scan rates (Fig. S2). According to the literature [40], the C_{cs} of MnO$_2$ in TTCP-Mn/GOS and TTCP-MnO$_2$ (Fig.S2) can be calculated and found to be about 741 and 611 F g^{-1}, respectively. The C_{cs} of MnO$_2$ decreases gradually with the increment of the scan rate, but the values of C_{cs} for TTCP-MnO$_2$/GOS are larger than that for TTCP-MnO$_2$ at all scan rates (Fig. 4B). For example at 100 mV s^{-1}, TTCP-MnO$_2$/GOS retains a C_{cs} of about 434 F g^{-1} (59 % of the initial C_{cs}) while TTCP-MnO$_2$ retains a C_{cs} of about 353 F g^{-1} (57 % of the initial C_{cs}).

From the discharged curves of TTCP-MnO$_2$/GOS at various current densities (Fig. 5A), it can be found that the C_{cs} for MnO$_2$ can reach to about 829 F g^{-1} at the discharged current density of 1 A g^{-1}, and that the discharged time decreases with the increment of the discharged current density. Furthermore, it is found that the discharged curves are almost linear at large current density while non-linear at small current density. It is well known that the capacitance of MnO$_2$ contains the electric double layer capacitance and Faradic capacitance. At large current density, the electric double layer capacitance is primary and the discharged curve is linear;

Fig. 6 The plots of the specific capacitance of MnO$_2$ versus the cycle numbers for TTCP-MnO$_2$ (a) and TTCP-MnO$_2$/GOS (b)

however, the Faradic capacitance will become important at the small current density. Therefore, the non-linear curve observed for 1.0 A g^{-1} can be attributed to the reduction of the material at low potential. The C_{cs} for MnO$_2$ deposited on TTCP (TTCP-MnO$_2$) is calculated to be 749 F g^{-1} according to the discharged curve shown in Fig. S3. From the repeated charge/discharge curves at 5.0 A g^{-1} (Fig. 5B), it is also found that the charged curves are almost symmetric to their discharged counterparts in the whole potential region. Furthermore, the sample of TTCP-MnO$_2$/GOS shows a longer charge/discharge time and less deviation from cutoff potential than that of TTCP-MnO$_2$. This may be that the contact between the active material and TTCP becomes loosen due to the volume change of MnO$_2$ caused by the ions insertion and deinsertion during the repeated charge/discharge process. However, the large porous structure makes TTCP-MnO$_2$/GOS avoided this defect. These results indicate that TTCP-MnO$_2$/GOS not only exhibits higher C$_{cs}$ but also higher stability compared with TTCP-MnO$_2$.

The EIS spectra (Fig.S4) show the small arc in the high-frequency region and almost linear portion at low-frequency region. The impedance spectra are analyzed by the software of ZView2 on the basis of the electrical equivalent circuit as shown in Fig.S4A. In the low-frequency region, the spike is almost vertical, indicating a pronounced capacitive behavior with small diffusion resistance. At very high frequency, the intercept on real axis represents a combined resistance (R_s) including intrinsic resistance of electrode materials, ionic resistance of electrolyte and contact resistance between electrode and current collector [41, 42]. The diameter of the semicircle corresponds to the charge-transfer resistance (R_{ct}) caused by Faradic reactions and electric double layer capacitor (C_{dl}) at the electrode/ electrolyte interface. The 45° sloped portion in the mediate frequency region, known as Warburg resistance (Z_w), is a result of the frequency dependence of electrolyte diffusion/transport into the porous electrodes [22] and C_L is the limit capacitance [42]. The EIS spectra exhibit identical R_s for TTCP-MnO$_2$ (0.70 Ω) and for TTCP-MnO$_2$/GOS (1.64 Ω) but smaller R_{ct} (7.74 Ω vs. 9.05 Ω) for TTCP-MnO$_2$/GOS electrode. Fig.S4B presents the C_{cs} obtained from EIS for the two samples [43], it is clear that the C_{cs} decreases with the increase of the frequency and behaves like a pure resistance in high-frequency region, and that TTCP-MnO$_2$/GOS exhibits a higher C_{cs} at low frequency compared with TTCP-MnO$_2$, which is consistent with the results obtained from CV and charge/discharge data. The relatively higher C_{cs} of TTCP-MnO$_2$/GOS may be mainly resulted from the high dispersion of MnO$_2$ on GOS and the large porous structure formed by the composite of MnO$_2$/GOS on TTCP, which make the active material possess large surface area and contact to electrolyte easy.

As the stability of the materials is a very important factor for the electrochemical capacitors' application, the stability of the two samples have been evaluated by using CV method at a scan rate of 50 mV s^{-1} and the results are shown in Fig. 6. It is found that the C_{sc} of TTCP-MnO$_2$ decreases slowly during the successive scan after it decreases from 410 (1st cycle) to about 350 F g^{-1} at the 100th cycle (Fig. 6A), while the C_{cs} of TTCP-MnO$_2$/GOS is kept constant or increases slightly after it decreases from 489 to about 400 F g^{-1} during the repeated 500 cycles (Fig. 6B). Finally, the C_{cs} retains 81.5 % of the initial value for TTCP-MnO$_2$/GOS and 82.3 % for TTCP-MnO$_2$ after 1,500 cycles. Furthermore, the C_{cs} of TTCP-MnO$_2$/GOS is obviously larger than that of TTCP-MnO$_2$ during the whole stability test process, which indicates that the incorporation of GOS into MnO$_2$ can improve the performance of the electrodes.

Conclusions

The hybrid of MnO$_2$/GOS has been electrochemically deposited on the TTCP by co-deposition in the PBS containing GOS and KMnO$_4$. The resulted MnO$_2$ is characterized to be birnessite and its morphology is strongly influenced by the presence of GOS. The MnO$_2$/GOS hybrid exhibits larger C_{cs} and higher stability than that of MnO$_2$ deposited on the TTCP, and may be used as electrodes in the supercapacitors with high performance.

References

1. Broughton JN, Brett MJ (2005) Electrochim Acta 50:4814–4819
2. Yan J, Fan ZJ, Wei T, Qian WZ, Zhang ML, Wei F (2010) Carbon 48:3825–3833
3. Simon P, Gogotsi Y (2008) Nat Mater 7:845–854
4. Jin M, Han GY, Chang YZ, Zhao H, Zhang HY (2011) Electrochim Acta 56:9838–9845
5. Wang XW, Liu SQ, Wang HY, Tu FY, Fang D, Li YH (2012) J Solid State Electrochem 16:3593–3602
6. Wei J, Nagarajan N, Zhitomirsky I (2007) J Mater Process Technol 186:356–361
7. Chang JK, Huang CH, Tsai WT, Deng MJ, Sun IW, Chen PY (2008) Electrochim Acta 53:4447–4453
8. Devaraj S, Munichandraiah N (2005) Electrochem Solid-State Lett 8(7):A373–A377
9. Hu CC, Tsou TW (2003) J Power Sources 115:179–186
10. Wei J, Zhitomirsky I (2008) Surf Eng 24:40–46
11. Lee SW, Kim JY, Chen S, Hammond PT, Shaohorn Y (2010) ACS Nano 4:3889–3896
12. Yu GH, Hu LB, Liu N, Wang HL, Vosgueritchian M, Yang Y, Cui Y, Bao ZN (2011) Nano Lett 11:4438–4442

13. Bordjiba T, Mohamedi M, Dao LH (2007) Nanotechnology 18(035202):5
14. Wang Y, Yu SF, Sun CY, Zhu TJ, Yang HY (2012) J Mater Chem 22: 17584–17588
15. Yuan LY, Lu XH, Xiao X, Zhai T, Dai JJ, Zhang FC, Hu B, Wang X, Gong L, Chen J, Hu CG, Tong YX, Zhou J, Wang ZL (2012) ACS Nano 6:656–661
16. Zhang LL, Wei TX, Wang WJ, Zhao XS (2009) Microporous Mesoporous Mater 123:260–267
17. Amade R, Jover E, Caglar B, Mutlu T, Bertran E (2011) J Power Sources 196:5779–5783
18. Geim AK, Novoselov KS (2007) Nat Mater 6:183–191
19. Guo S, Dong S (2011) Chem Soc Rev 40:2644–2672
20. Chen S, Zhu JW, Wu XD, Han QF, Wang X (2010) ACS Nano 4: 2822–2830
21. Zhao X, Zhang LL, Murali S, Stoller MD, Zhang QH, Zhu YW, Ruoff RS (2012) ACS Nano 6:5404–5412
22. Cheng Q, Tang J, Ma J, Zhang H, Shinya N, Qin LC (2011) Carbon 49:2917–2925
23. Fan ZJ, Zhao QK, Li TY, Yan J, Ren YM, Feng J, Wei T (2012) Carbon 50:1699–1712
24. Chang JK, Tsai WT (2003) J Electrochem Soc 150:A1333–A1338
25. Chang JK, Tsai WT (2004) J Appl Electrochem 34:953–961
26. Chou SL, Wang JZ, Chew SY, Liu HK, Dou SX (2008) Electrochem Commun 10:1724–1727
27. Wu MS, Guo ZS, Jow JJ (2010) J Phys Chem C 114:21861–21867
28. Zhu CZ, Guo SJ, Fang YX, Han L, Wang EK, Dong SJ (2011) Nano Res 4(7):648–657
29. Peng XY, Liu XX, Diamond D, Lau KT (2011) Carbon 49:3488–3496
30. Yang J, Gunasekaran S (2013) Carbon 51:36–44
31. Chang YZ, Han GY, Li MY, Gao F (2011) Carbon 49:5158–5165
32. Sheng KX, Xu YX, Li C, Shi GQ (2011) New Carbon Mater 26:9–15
33. Zhao H, Han GY, Chang YZ, Li MY, Li YP (2013) Electrochim Acta 91:50–57
34. Raymundo-Pinero E, Gao Q, Beguin F (2013) Carbon 61:278–283
35. Fu DY, Han GY, Chang YZ, Dong JH (2012) Mater Chem Phys 132: 673–681
36. Bonhomme F, Lassegues JC, Servant L (2001) J Electrochem Soc 148:E450–E458
37. Zhang XH, Li BX, Liu CY, Chu QX, Liu FY, Wang XF, Chen HW, Liu XY (2013) Mater Res Bull 48:2696–2701
38. Julien C, Massot M, Baddour-Hadjean R, Franger S, Bach S, Pereira-Ramos JP (2003) Solid State Ionics 159:345–356
39. Fu DY, Han GY, Yang FF, Zhang TW, Chang YZ, Liu FF (2013) Appl Surf Sci 283:654–659
40. Zhang L, Shi GQ (2011) J Phys Chem C 115:17206–17212
41. Khomenko V, Raymundo-Pinero E, Beguin F (2006) Appl Phys A 82:567–573
42. Wang JG, Yang Y, Huang ZH, Kang FY (2013) Carbon 61:190–199
43. Jin M, Liu YY, Li YL, Chang YZ, Fu DY, Zhao H, Han GY (2011) J Appl Polym Sci 122:3415–3422